Air Force Institute of Technology

AFIT Scholar

Faculty Publications

12-30-2013

Scattering of a Partially-coherent Wave from a Material Circular Cylinder

Milo W. Hyde IV
Air Force Institute of Technology

Andrew E. Bogle

Michael J. Havrilla
Air Force Institute of Technology

Follow this and additional works at: https://scholar.afit.edu/facpub

Part of the Electromagnetics and Photonics Commons

Recommended Citation

Hyde IV, M. W., Bogle, A. E., & Havrilla, M. J. (2013). Scattering of a partially-coherent wave from a material circular cylinder. Optics Express, 21(26), 32327. https://doi.org/10.1364/OE.21.032327

Scattering of a partially-coherent wave from a material circular cylinder

Milo W. Hyde IV,[*] **Andrew E. Bogle, and Michael J. Havrilla**

Air Force Institute of Technology, 2950 Hobson Way, Dayton, OH 45433, USA

[*]*milo.hyde@afit.edu*

Abstract: The case of a partially-coherent wave scattered from a material circular cylinder is investigated. Expressions for the TM^z and TE^z scattered-field cross-spectral density functions are derived by utilizing the plane-wave spectrum representation of electromagnetic fields and cylindrical wave transformations. From the analytical scattered-field cross-spectral density functions, the mean scattering widths are derived and subsequently validated via comparison with those computed from Method of Moments Monte Carlo simulations. The analytical relations as well as the simulation results are discussed and physically interpreted. Key insights are noted and subsequently analyzed.

References and links

1. E. Wolf, *Introduction to the Theory of Coherence and Polarization of Light* (Cambridge University, 2007).
2. A. Ishimaru, *Electromagnetic Wave Propagation, Radiation, and Scattering* (Prentice Hall, 1991).
3. R. Harrington, *Time-Harmonic Electromagnetic Fields* (IEEE, 2001).
4. R. Harrington, *Field Computation by Moment Methods* (IEEE, 1993).
5. A. Peterson, S. Ray, and R. Mittra, *Computational Methods for Electromagnetics* (IEEE, 1997).
6. C. A. Balanis, *Advanced Engineering Electromagnetics*, 2nd ed. (Wiley, 2012).
7. J. R. Wait, "Scattering of a plane wave from a circular dielectric cylinder at oblique incidence," Can. J. Phys. **33**, 189–195 (1955).
8. M. Kerker and E. Matijević, "Scattering of electromagnetic waves from concentric infinite cylinders," J. Opt. Soc. Am. **51**, 506–508 (1961).
9. J. Richmond, "Scattering by a dielectric cylinder of arbitrary cross section shape," IEEE Trans. Antennas Propag. **13**, 334–341 (1965).
10. B. H. Henin, A. Z. Elsherbeni, and M. H. Al Sharkawy, "Oblique incidence plane wave scattering from an array of circular dielectric cylinders," Prog. Electromagn. Res. **68**, 261–279 (2007).
11. S. Marin, "Computing scattering amplitudes for arbitrary cylinders under incident plane waves," IEEE Trans. Antennas Propag. **30**, 1045–1049 (1982).
12. A. Madrazo and M. Nieto-Vesperinas, "Scattering of electromagnetic waves from a cylinder in front of a conducting plane," J. Opt. Soc. Am. A **12**, 1298–1309 (1995).
13. R. Borghi, F. Gori, M. Santarsiero, F. Frezza, and G. Schettini, "Plane-wave scattering by a perfectly conducting circular cylinder near a plane surface: cylindrical-wave approach," J. Opt. Soc. Am. A **13**, 483–493 (1996).
14. R. Borghi, F. Gori, M. Santarsiero, F. Frezza, and G. Schettini, "Plane-wave scattering by a set of perfectly conducting circular cylinders in the presence of a plane surface," J. Opt. Soc. Am. A **13**, 2441–2452 (1996).
15. G. Videen and D. Ngo, "Light scattering from a cylinder near a plane interface: theory and comparison with experimental data," J. Opt. Soc. Am. A **14**, 70–78 (1997).
16. M. Tateiba and Z. Q. Meng, "Wave scattering from conducting bodies embedded in random media—theory and numerical results," Prog. Electromagn. Res. **14**, 317–361 (1996).
17. Z. Q. Meng and M. Tateiba, "Radar cross sections of conducting elliptic cylinders embedded in strong continuous random media," Waves Random Complex Media **6**, 335–345 (1996).

18. M. A. Ashraf and A. A. Rizvi, "Electromagnetic scattering from a random cylinder by moments method," J. Electromagn. Waves Appl. **25**, 467–480 (2011).
19. S. Ahmed and Q. A. Naqvi, "Electromagnetic scattering from parallel perfect electromagnetic conductor cylinders of circular cross-sections using an iterative procedure," J. Electromagn. Waves Appl. **22**, 987–1003 (2008).
20. M. Kluskens and E. Newman, "Scattering by a multilayer chiral cylinder," IEEE Trans. Antennas Propag. **39**, 91–96 (1991).
21. J. Geng, R. W. Ziolkowski, R. Jin, and X. Liang, "Active cylindrical coated nano-particle antennas: polarization-dependent scattering properties," J. Electromagn. Waves Appl. **27**, 1392–1406 (2013).
22. T. Kojima and Y. Yanagiuchi, "Scattering of an offset two-dimensional Gaussian beam wave by a cylinder," J. Appl. Phys. **50**, 41–46 (1979).
23. S. Kozaki, "A new expression for the scattering of a Gaussian beam by a conducting cylinder," IEEE Trans. Antennas Propag. **30**, 881–887 (1982).
24. M. Yokota, T. Takenaka, and O. Fukumitsu, "Scattering of a Hermite-Gaussian beam mode by parallel dielectric circular cylinders," J. Opt. Soc. Am. A **3**, 580–586 (1986).
25. Z. W. L. Guo, "Electromagnetic scattering from a multilayered cylinder arbitrarily located in a Gaussian beam, a new recursive algorithms," Prog. Electromagn. Res. **18**, 317–333 (1998).
26. X. M. Sun, H. H. Wang, and H. Y. Zhang, "Scattering by an infinite cylinder arbitrarily illuminated with a couple of Gaussian beams," J. Electromagn. Waves Appl. **24**, 1329–1339 (2010).
27. A. Elsherbeni, M. Hamid, and G. Tian, "Iterative scattering of a Gaussian beam by an array of circular conducting and dielectric cylinders," J. Electromagn. Waves Appl. **7**, 1323–1342 (1993).
28. H. Zhang and Y. Han, "Scattering of shaped beam by an infinite cylinder of arbitrary orientation," J. Opt. Soc. Am. B **25**, 131–135 (2008).
29. K. F. Ren, G. Gréhan, and G. Gouesbet, "Scattering of a Gaussian beam by an infinite cylinder in the framework of generalized Lorenz-Mie theory: formulation and numerical results," J. Opt. Soc. Am. A **14**, 3014–3025 (1997).
30. G. Gouesbet, "Interaction between an infinite cylinder and an arbitrary-shaped beam," Appl. Opt. **36**, 4292–4304 (1997).
31. G. Gouesbet, "Scattering of higher-order Gaussian beams by an infinite cylinder," J. Opt. **28**, 45–65 (1997).
32. E. Zimmermann, R. Dändliker, N. Souli, and B. Krattiger, "Scattering of an off-axis Gaussian beam by a dielectric cylinder compared with a rigorous electromagnetic approach," J. Opt. Soc. Am. A **12**, 398–403 (1995).
33. H. Zhang, Z. Huang, and Y. Shi, "Internal and near-surface electromagnetic fields for a uniaxial anisotropic cylinder illuminated with a Gaussian beam," Opt. Express **21**, 15645–15653 (2013).
34. M. L. Marasinghe, M. Premaratne, and D. M. Paganin, "Coherence vortices in Mie scattering of statistically stationary partially coherent fields," Opt. Express **18**, 6628–6641 (2010).
35. M. L. Marasinghe, M. Premaratne, D. M. Paganin, and M. A. Alonso, "Coherence vortices in Mie scattered nonparaxial partially coherent beams," Opt. Express **20**, 2858–2875 (2012).
36. D. G. Fischer, T. van Dijk, T. D. Visser, and E. Wolf, "Coherence effects in Mie scattering," J. Opt. Soc. Am. A **29**, 78–84 (2012).
37. J. Lindberg, T. Setälä, M. Kaivola, and A. T. Friberg, "Spatial coherence effects in light scattering from metallic nanocylinders," J. Opt. Soc. Am. A **23**, 1349–1358 (2006).
38. L. Mandel and E. Wolf, *Optical Coherence and Quantum Optics* (Cambridge University, 1995).
39. J. W. Goodman, *Statistical Optics* (Wiley, 1985).
40. B. G. Hoover and V. L. Gamiz, "Coherence solution for bidirectional reflectance distributions of surfaces with wavelength-scale statistics," J. Opt. Soc. Am. A **23**, 314–328 (2006).
41. T. Hansen and A. Yaghjian, *Plane-Wave Theory of Time-Domain Fields* (IEEE, 1999).
42. M. Nieto-Vesperinas, *Scattering and Diffraction in Physical Optics* (World Scientific, 2006), 2nd ed.
43. C. A. Mack, "Analytic form for the power spectral density in one, two, and three dimensions," J. Micro/Nanolithogr. MEMS MOEMS **10**, 040501 (2011).
44. It should be noted that no source can be spatially completely incoherent, i.e., $\ell_s = 0$. The physical minimum value of ℓ_s is on the order of λ [1].
45. X. Xiao and D. Voelz, "Wave optics simulation approach for partial spatially coherent beams," Opt. Express **14**, 6986–6992 (2006).
46. RefractiveIndex.INFO, "RefractiveIndex.INFO Refractive index database, http://refractiveindex.info," (Retrieved on Jun. 25, 2013).

1. Introduction

The scattering of waves from cylinders is a classic problem in electromagnetics (EM). Because cylinders closely model man-made objects such as aircraft, rockets, antennas, etc. as well as biological structures [2], they have received much attention in the literature including several common EM texts [3–6]. The early accounts on the subject considered plane-wave scattering [7–9].

More recent treatments consider plane-wave scattering from arrays of cylinders [10, 11], scattering from cylinders in front of ground planes [12–15], scattering from cylinders embedded in random media [16, 17], scattering from random cylinders [18], and scattering from cylinders composed of complex media [19–21].

Beginning in the late 1970s and into the 1980s, Gaussian-beam scattering from cylinders began to appear in the literature [22–24]. Since then, the amount of published research dealing with Gaussian beams and cylinders has increased greatly with the proliferation of laser radar and directed energy systems [25–33].

Although much effort has been devoted to plane-wave and Gaussian-beam scattering from cylinders, little has been devoted to partially-coherent wave scattering from cylinders. This topic is germane considering that coherent waves lose coherence as they propagate through random media, such as Earth's atmosphere, natural bodies of water, biological tissues, and soil. The majority of the relevant work in the scattering of partially-coherent waves from cylinders has actually focused on spheres [34–36]. Only one paper known to the authors deals with cylinders. Lindberg *et al.* [37] used the coherent-mode representation of partially-coherent fields and a numerical technique very similar to the Method of Moments (MoM) to analyze the scattering from metallic nanocylinders.

In this work, the scattering of a partially-coherent wave from a material cylinder is investigated. In contrast to the previous effort discussed above, the partially-coherent incident field is written in terms of its plane-wave spectrum in a transverse plane situated away from the cylinder. The resulting expression is then expanded in terms of cylindrical wave functions. Continuity of the transverse electric and magnetic fields is then enforced at the surface of the material cylinder producing expressions for the unknown cylindrical wave function weights. With these weights, the autocorrelation of the scattered field, termed the cross-spectral density (CSD) function, is derived and discussed. Both the TM^z and TE^z scattered-field CSD functions are presented.

To validate the analytical TM^z and TE^z scattered-field CSD functions, the general CSD function expressions are specialized to the case of a partially-coherent plane-wave incident field. From these plane-wave CSD relations, the mean two-dimensional radar cross sections, i.e., the mean scattering widths, are derived. The analytical mean scattering widths are subsequently compared to those computed from MoM Monte Carlo simulations. These results are presented and physically analyzed. A summary of the presented work and key physical findings are provided to conclude this paper.

2. Methodology

The pertinent scattering geometry for this research is shown in Fig. 1. The figure depicts a material cylinder (of radius a, permittivity ε, and permeability μ) illuminated by a partially-coherent wave (shown as a partially-coherent plane wave for ease of visualization). The cylinder and the incident field are assumed to be invariant in the z direction. The partially-coherent incident field is emitted from the η-z plane (termed the source plane hereafter) whose origin is located at $(-x_s, y_s)$. The two spatial-domain vectors emanating from the source-plane origin, $\boldsymbol{\rho}_{\xi\eta} = \hat{\boldsymbol{x}} x_s - \hat{\boldsymbol{y}} y_s$ and $\boldsymbol{s} = \boldsymbol{\rho}_{\xi\eta} + \boldsymbol{\rho}$, point to the center of the cylinder and to any location in space $\xi \geq 0$, respectively. The wavenumber vector $\boldsymbol{k}^i = \hat{\boldsymbol{\xi}} k_{\xi}^i + \hat{\boldsymbol{\eta}} k_{\eta}^i$ denotes the direction of a plane wave emanating from the source-plane origin. The vector $\boldsymbol{k}^i$ makes the angle α with respect to the ξ axis.

The partially-coherent incident field is treated as a random process, statistically defined via its autocorrelation function $\langle E^i(\eta_1) E^{i*}(\eta_2) \rangle$. In the space-time domain, this expression is commonly referred to as the mutual coherence function (MCF) $\Gamma^i(\eta_1, \eta_2, \tau)$ [1, 38]. If the random
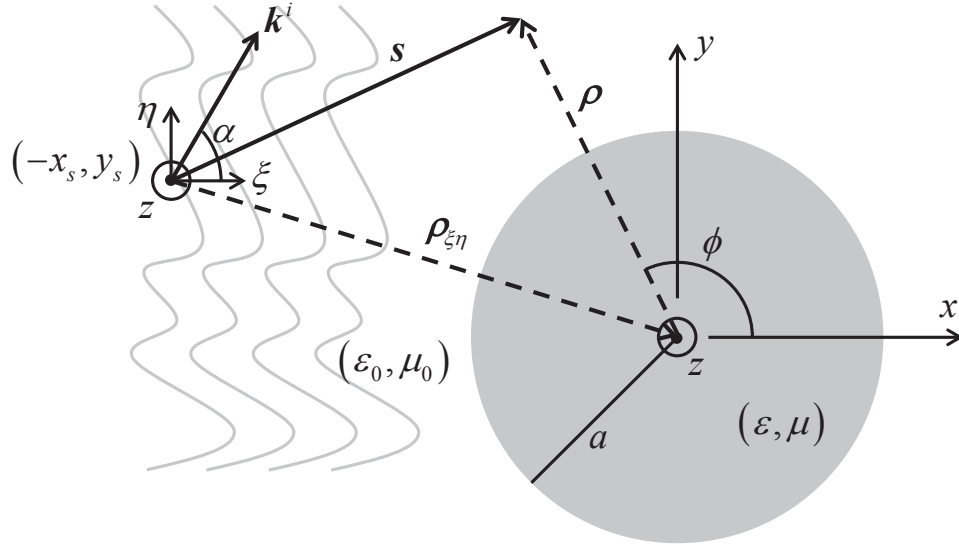
Fig. 1. Two-dimensional scattering geometry (invariant in the z direction) of a material (ε, μ) circular cylinder (of radius a) illuminated by a partially-coherent wave. The partially-coherent incident field is emitted from the η-z plane whose origin is located at $(-x_s, y_s)$. The spatial-domain vectors emanating from the source-plane origin, $\boldsymbol{\rho}_{\xi\eta} = \hat{\mathbf{x}} x_s - \hat{\mathbf{y}} y_s$ and $\boldsymbol{s} = \boldsymbol{\rho}_{\xi\eta} + \boldsymbol{\rho}$, point to the center of the cylinder and to any location in space $\xi \geq 0$, respectively. The wavenumber vector $\boldsymbol{k}^i = \hat{\boldsymbol{\xi}} k_\xi^i + \hat{\boldsymbol{\eta}} k_\eta^i$ denotes the direction of a plane wave emanating from the source-plane origin. The vector $\boldsymbol{k}^i$ makes the angle α with respect to the ξ axis.

field is wide-sense stationary (assumed in this work), it is most convenient to work in the space-frequency domain, where

$$W^i(\eta_1, \eta_2, \omega) = \left\langle E^i(\eta_1, \omega) E^{i*}(\eta_2, \omega) \right\rangle = \frac{1}{2\pi} \int_{-\infty}^{\infty} \Gamma^i(\eta_1, \eta_2, \tau) e^{j\omega\tau} d\tau \tag{1}$$

is the CSD function [1,38]. Note that if the field satisfies the quasi-monochromatic conditions (a common assumption in traditional studies of coherence) [39], the CSD is essentially equivalent to the MCF [40].

2.1. TM^z scattered-field CSD function

For TM^z polarization, the incident field in the source plane takes the form

$$\boldsymbol{E}^i = \hat{\mathbf{z}} E_z^i(\eta), \tag{2}$$

where the dependence of the field on the radian frequency ω has been omitted for brevity. Utilizing the plane-wave spectrum representation of electromagnetic fields [41], the incident electric field becomes

$$\begin{aligned}
\boldsymbol{E}^i &= \frac{1}{2\pi} \int_{-\infty}^{\infty} \boldsymbol{T}_e^i(k_\eta^i) e^{-j\boldsymbol{k}^i \cdot \boldsymbol{s}} dk_\eta^i \quad \xi \geqslant 0 \\
&= \hat{\mathbf{z}} \frac{k_0}{2\pi} \int_{\Gamma} T_{ez}^i(\alpha) \cos(\alpha) e^{-jk_0 x_s \cos(\alpha)} e^{jk_0 y_s \sin(\alpha)} e^{-jk_0 \rho \cos(\phi-\alpha)} d\alpha
\end{aligned}, \tag{3}$$

where Γ is the contour in the complex α plane defined by $(-\pi/2 - j\infty, -\pi/2)$, $[-\pi/2, \pi/2]$, and $(\pi/2, \pi/2 + j\infty)$. The contribution to the integral from the real-axis portion of Γ corresponds physically to forward propagating waves; whereas, the contributions from the complex portions of Γ correspond to evanescent waves [42]. In this work, it is assumed that the source plane is sufficiently far from the cylinder such that the evanescent wave contributions can be neglected. The remaining undefined symbol in Eq. (3) is

$$T_{ez}^i \left(k_\eta^i \right) = \int_{-\infty}^{\infty} E_z^i (\eta) \, e^{jk_\eta^i \eta} \mathrm{d}\eta. \tag{4}$$

Note that $k_\eta^i = k_0 \sin(\alpha)$.

Expressing the $\exp[-jk_0\rho \cos(\phi - \alpha)]$ in terms of cylindrical wave functions [2, 3] yields

$$\boldsymbol{E}^i = \hat{z} \frac{k_0}{2\pi} \sum_{n=-\infty}^{\infty} j^{-n} J_n (k_0\rho) e^{jn\phi} \int_{-\pi/2}^{\pi/2} T_{ez}^i (\alpha) \cos(\alpha) e^{-jk_0 x_s \cos(\alpha)} e^{jk_0 y_s \sin(\alpha)} e^{-jn\alpha} \mathrm{d}\alpha, \tag{5}$$

where J_n is a first-kind Bessel function of order n. Hereafter, the integral over α is referred to as $\mathscr{I}_n^{\mathrm{TM}}$. The transverse, incident magnetic field H_ϕ^i can now be found by utilizing Faraday's law:

$$H_\phi^i = \frac{k_0}{2\pi} \frac{1}{j\eta_0} \sum_{n=-\infty}^{\infty} j^{-n} \dot{J}_n (k_0\rho) e^{jn\phi} \mathscr{I}_n^{\mathrm{TM}}, \tag{6}$$

where $\dot{J}_n$ represents the derivative of the Bessel function with respect to its argument. The scattered and transmitted, transverse electric and magnetic fields take the forms

$$
\begin{aligned}
E_z^s &= \sum_{n=-\infty}^{\infty} b_n H_n^{(2)} (k_0\rho) & H_\phi^s &= \frac{1}{j\eta_0} \sum_{n=-\infty}^{\infty} b_n \dot{H}_n^{(2)} (k_0\rho) \\
E_z^t &= \sum_{n=-\infty}^{\infty} c_n J_n (k\rho) & H_\phi^t &= \frac{1}{j\eta} \sum_{n=-\infty}^{\infty} c_n \dot{J}_n (k\rho)
\end{aligned}
\tag{7}
$$

where $H_n^{(2)}$ is a nth-order Hankel function of the second kind and physically represents outgoing cylindrical waves and b_n and c_n are unknown complex amplitudes.

Expressions for b_n and c_n are found by enforcing the continuity of transverse electric and magnetic fields at the surface of the cylinder, i.e., $\rho = a$. In the discussion to follow, only b_n is considered since the scattered field is paramount here. Imposing the boundary condition and subsequent simplification yields

$$b_n = \frac{-k_0}{2\pi} j^{-n} e^{jn\phi} R_n^{\mathrm{TM}} \mathscr{I}_n^{\mathrm{TM}}, \tag{8}$$

where

$$R_n^{\mathrm{TM}} = \frac{\eta J_n (ka) \dot{J}_n (k_0 a) - \eta_0 J_n (k_0 a) \dot{J}_n (ka)}{\eta J_n (ka) \dot{H}_n^{(2)} (k_0 a) - \eta_0 H_n^{(2)} (k_0 a) \dot{J}_n (ka)} \tag{9}$$

and physically acts as a reflection coefficient. For good-conducting cylinders, i.e., $\varepsilon \to -j\infty$ and $\mu = \mu_0$, it is easy to show that $R_n^{\mathrm{TM}} \to J_n (k_0 a)/H_n^{(2)} (k_0 a)$. Note that this is the same reflection coefficient that one would derive assuming a perfect electric conductor (PEC) cylinder.

With an expression for b_n and thus E_z^s from Eq. (7), the relation for the scattered-field CSD function immediately follows:

$$
\begin{aligned}
W^s(\boldsymbol{\rho}_1, \boldsymbol{\rho}_2, \omega) &= \sum_{n=-\infty}^{\infty} \sum_{m=-\infty}^{\infty} \langle b_n(\phi_1) b_m^*(\phi_2) \rangle H_n^{(2)}(k_0 \rho_1) H_m^{(1)}(k_0 \rho_2) \\
&= \frac{k_0^2}{(2\pi)^2} \sum_{n=-\infty}^{\infty} \sum_{m=-\infty}^{\infty} \left\langle \mathscr{I}_n^{\mathrm{TM}} \mathscr{I}_m^{\mathrm{TM}*} \right\rangle \mathrm{j}^{m-n} e^{\mathrm{j}(n\phi_1 - m\phi_2)} \\
&\quad R_n^{\mathrm{TM}} R_m^{\mathrm{TM}*} H_n^{(2)}(k_0 \rho_1) H_m^{(1)}(k_0 \rho_2)
\end{aligned}
\tag{10}
$$

The incident-field term is

$$
\begin{aligned}
\left\langle \mathscr{I}_n^{\mathrm{TM}} \mathscr{I}_m^{\mathrm{TM}*} \right\rangle &= \int_{-\pi/2}^{\pi/2} \int_{-\pi/2}^{\pi/2} \cos(\alpha_1) \cos(\alpha_2) \left\langle T_{ez}^i(\alpha_1) T_{ez}^{i*}(\alpha_2) \right\rangle \\
&\quad e^{-\mathrm{j}k_0 x_s [\cos(\alpha_1) - \cos(\alpha_2)]} e^{\mathrm{j}k_0 y_s [\sin(\alpha_1) - \sin(\alpha_2)]} e^{-\mathrm{j}(n\alpha_1 - m\alpha_2)} \, \mathrm{d}\alpha_1 \, \mathrm{d}\alpha_2 \\
&= \frac{1}{k_0^2} \int_{-k_0}^{k_0} \int_{-k_0}^{k_0} \left\langle T_{ez}^i\left(k_{\eta 1}^i\right) T_{ez}^{i*}\left(k_{\eta 2}^i\right) \right\rangle \\
&\quad e^{-\mathrm{j}x_s\left(k_{\xi 1}^i - k_{\xi 2}^i\right)} e^{\mathrm{j}y_s\left(k_{\eta 1}^i - k_{\eta 2}^i\right)} e^{-\mathrm{j}\left[n\sin^{-1}\left(k_{\eta 1}^i/k_0\right) - m\sin^{-1}\left(k_{\eta 2}^i/k_0\right)\right]} \mathrm{d}k_{\eta 1}^i \mathrm{d}k_{\eta 2}^i
\end{aligned}
\tag{11}
$$

2.2. Physical discussion

Note that Eq. (10) is remarkably physical. If one ignores the incident-field term, the remaining expression in Eq. (10) is the scattered-field CSD function for a coherent plane wave incident on a material cylinder. Thus, Eq. (11) can be thought of as a "filter," which is subsequently "convolved" with the response of the system to a coherent plane-wave input.

The behavior of the "filter" can be complicated depending on the form of the incident-field CSD function Eq. (1); however, insight can be gleaned into its behavior by considering a partially-coherent plane-wave incident field:

$$
W_{\mathrm{PW}}^i(\eta_1, \eta_2, \omega) = E_0^2 C(\eta_1 - \eta_2; \ell_s),
\tag{12}
$$

where E_0 is the magnitude of the incident field, ℓ_s is the spatial correlation, or coherence radius, and $C(\eta_1 - \eta_2; \ell_s)$ is the normalized correlation, or coherence function. For natural random processes, e.g., atmospheric turbulence, this function decreases from unity at $\eta_1 - \eta_2 = 0$. Common choices for C are exponentially decaying functions with powers between one and two [43].

As $\ell_s \to \infty$, $\left\langle T_{ez}^i(\alpha_1) T_{ez}^{i*}(\alpha_2) \right\rangle \to \delta(\alpha_1 - \alpha_2)$ (recall Eq. (4)) resulting in W^s Eq. (10) converging to the traditional plane-wave scattered-field solution. As $\ell_s \to 0$ [44], $\left\langle T_{ez}^i(\alpha_1) T_{ez}^{i*}(\alpha_2) \right\rangle \to 1$ yielding an incident-field term which "filters out" the fine lobing structure characteristic of the traditional plane-wave scattered-field pattern. This makes physical sense when one considers that the scattered-field lobing pattern is caused by interference of the field upon scattering from the cylinder. Since incoherent fields do not interfere, one should expect a more homogeneous scattered-field pattern with a partially-coherent incident field than that obtained with a fully-coherent incident wave.

2.3. TM^z mean scattering width

Setting $\boldsymbol{\rho}_1 = \boldsymbol{\rho}_2 = \boldsymbol{\rho}$, substituting Eq. (12) into Eq. (11), taking the limit of Eq. (10) as $\rho \to \infty$, and subsequent simplification yields the TM^z far-zone plane-wave scattered-field spectral-

density S_{FF}^s function:

$$
\begin{aligned}
W_{\mathrm{FF}}^s(\boldsymbol{\rho},\boldsymbol{\rho},\omega) &= S_{\mathrm{FF}}^s(\boldsymbol{\rho},\omega) \\
&= \frac{E_0^2}{\pi^2 k_0 \rho} \sum_{n=-\infty}^{\infty} \sum_{m=-\infty}^{\infty} R_n^{\mathrm{TM}} R_m^{\mathrm{TM}*} e^{\mathrm{j}(n-m)\phi} \\
&\quad \int_{-k_0}^{k_0} e^{-\mathrm{j}(n-m)\sin^{-1}\left(k_\eta^i/k_0\right)} \int_{-\infty}^{\infty} C(\eta;\ell_s) e^{\mathrm{j}k_\eta^i \eta}\,\mathrm{d}\eta\,\mathrm{d}k_\eta^i
\end{aligned}
\tag{13}
$$

The mean scattering width can easily be found by applying its definition, namely,

$$
\overline{\sigma_{\mathrm{2D}}}(\omega) = \lim_{\rho\to\infty} 2\pi\rho \frac{\left\langle \left| E_z^s(\boldsymbol{\rho},\omega) \right|^2 \right\rangle}{\left\langle \left| E_z^i(\eta,\omega) \right|^2 \right\rangle} = \lim_{\rho\to\infty} 2\pi\rho \frac{\left\langle S_{\mathrm{FF}}^s(\boldsymbol{\rho},\omega) \right\rangle}{\left\langle W_{\mathrm{PW}}^i(\eta,\eta,\omega) \right\rangle}.
\tag{14}
$$

The integral over η in Eq. (13) is nothing more than the Fourier transform of the coherence function making it akin to the power spectral density [39]. Unfortunately, after the Fourier transform is computed, it is not possible to simplify the remaining k_η^i integral further. For the results presented in Section 3, adaptive Gauss-Kronrod quadrature is used to numerically compute the remaining k_η^i integral.

Note that by specifying a partially-coherent plane-wave incident field, the scattered-field CSD function no longer depends on the location of the source plane. Physically, this makes sense since plane-wave fields are infinite in extent. Mathematically, this location invariance manifests as a result of the form of Eq. (12), where statistical homogeneity, viz., the spatial counterpart of wide-sense stationarity, is implied. This location invariance property should result for all statistically homogenous incident fields. For more complicated incident fields, such as partially-coherent Gaussian beams, the scattered-field CSD function will, in general, not be independent of the source-plane location.

2.4. TE^z scattered-field CSD function

Since many of the details in the TE^z scattered-field CSD function derivation are similar to those just presented for the TM^z case, only the major differences are presented here. For the TE^z polarization, it is most convenient to work with the magnetic field, i.e.,

$$
\begin{aligned}
\boldsymbol{H}^i = \hat{\boldsymbol{z}} H_z^i(\eta) &= \hat{\boldsymbol{z}} \frac{1}{2\pi} \int_{-\infty}^{\infty} T_{hz}^i\left(k_\eta^i\right) e^{-\mathrm{j}\boldsymbol{k}^i\cdot\boldsymbol{s}}\,\mathrm{d}k_\eta^i \quad \xi \geqslant 0 \\
&= \hat{\boldsymbol{z}} \frac{k_0}{2\pi} \sum_{n=-\infty}^{\infty} \mathrm{j}^{-n} J_n(k_0\rho) e^{\mathrm{j}n\phi} \mathscr{I}_n^{\mathrm{TE}}
\end{aligned}
\tag{15}
$$

where $\mathscr{I}_n^{\mathrm{TE}}$ is the same as $\mathscr{I}_n^{\mathrm{TM}}$ except that $T_{ez}^i(\alpha)$ is replaced with $T_{hz}^i(\alpha)$. The transverse, incident electric field E_ϕ^i can be found by utilizing Ampere's law, viz.,

$$
E_\phi^i = \frac{-k_0}{2\pi} \frac{\eta_0}{\mathrm{j}} \sum_{n=-\infty}^{\infty} \mathrm{j}^{-n} J_n(k_0\rho) e^{\mathrm{j}n\phi} \mathscr{I}_n^{\mathrm{TE}}.
\tag{16}
$$

The scattered and transmitted, transverse magnetic and electric fields take the forms

$$
\begin{aligned}
H_z^s &= \sum_{n=-\infty}^{\infty} b_n H_n^{(2)}(k_0\rho) & E_\phi^s &= \frac{-\eta_0}{\mathrm{j}} \sum_{n=-\infty}^{\infty} b_n \dot{H}_n^{(2)}(k_0\rho) \\
H_z^t &= \sum_{n=-\infty}^{\infty} c_n J_n(k\rho) & E_\phi^t &= \frac{-\eta}{\mathrm{j}} \sum_{n=-\infty}^{\infty} c_n \dot{J}_n(k\rho)
\end{aligned}
\tag{17}
$$

Enforcing the continuity of the transverse electric and magnetic fields at the surface of the cylinder yields the following expression for b_n:

$$b_n = \frac{-k_0}{2\pi} \mathrm{j}^{-n} e^{\mathrm{j}n\phi} R_n^{\mathrm{TE}} \mathscr{I}_n^{\mathrm{TE}}, \tag{18}$$

where

$$R_n^{\mathrm{TE}} = \frac{\eta J_n(k_0 a) \dot{J}_n(ka) - \eta_0 J_n(ka) \dot{J}_n(k_0 a)}{\eta H_n^{(2)}(k_0 a) \dot{J}_n(ka) - \eta_0 J_n(ka) \dot{H}_n^{(2)}(k_0 a)}. \tag{19}$$

For good-conducting cylinders, $R_n^{\mathrm{TE}} \rightarrow \dot{J}_n(k_0 a)/\dot{H}_n^{(2)}(k_0 a)$, or the same reflection coefficient that one would derive assuming a PEC cylinder.

With b_n, the TE^z scattered-field CSD function is

$$
\begin{aligned}
W^s(\boldsymbol{\rho}_1, \boldsymbol{\rho}_2, \omega) &= \eta_0^2 \sum_{n=-\infty}^{\infty} \sum_{m=-\infty}^{\infty} \langle b_n(\phi_1) b_m^*(\phi_2) \rangle \dot{H}_n^{(2)}(k_0\rho_1) \dot{H}_m^{(1)}(k_0\rho_2) \\
&= \eta_0^2 \frac{k_0^2}{(2\pi)^2} \sum_{n=-\infty}^{\infty} \sum_{m=-\infty}^{\infty} \left\langle \mathscr{I}_n^{\mathrm{TE}} \mathscr{I}_m^{\mathrm{TE}*} \right\rangle \mathrm{j}^{m-n} e^{\mathrm{j}(n\phi_1 - m\phi_2)} \\
&\qquad R_n^{\mathrm{TE}} R_m^{\mathrm{TE}*} \dot{H}_n^{(2)}(k_0\rho_1) \dot{H}_m^{(1)}(k_0\rho_2)
\end{aligned} \tag{20}
$$

Recall that $\mathscr{I}_n^{\mathrm{TE}}$ is in terms of T_{hz}^i and therefore $\left\langle \mathscr{I}_n^{\mathrm{TE}} \mathscr{I}_m^{\mathrm{TE}*} \right\rangle$ includes the moment $\left\langle T_{hz}^i(\alpha_1) T_{hz}^{i*}(\alpha_2) \right\rangle$. In general, the CSD function Eq. (1) is defined in terms of the electric field. Thus, to proceed further, a relation must be found between T_{hz}^i and $\boldsymbol{T}_e^i$. This relation can be derived using Faraday's law and is

$$\boldsymbol{T}_h^i = \frac{\boldsymbol{k}^i \times \boldsymbol{T}_e^i}{\omega\mu_0} = \hat{z} \frac{T_{e\eta}^i}{\eta_0 \cos(\alpha)}, \tag{21}$$

where it is assumed that the incident electric field in the source plane takes the form $\boldsymbol{E}^i = \hat{\eta} E_\eta^i(\eta)$. Utilizing the above relation, the incident-field term in Eq. (20) becomes

$$
\begin{aligned}
\left\langle \mathscr{I}_n^{\mathrm{TE}} \mathscr{I}_m^{\mathrm{TE}*} \right\rangle &= \frac{1}{\eta_0^2} \int_{-k_0}^{k_0} \int_{-k_0}^{k_0} \frac{\left\langle T_{e\eta}^i\left(k_{\eta 1}^i\right) T_{e\eta}^{i*}\left(k_{\eta 2}^i\right) \right\rangle}{k_{\xi 1}^i k_{\xi 2}^i} \\
&\quad e^{-\mathrm{j}x_s\left(k_{\xi 1}^i - k_{\xi 2}^i\right)} e^{\mathrm{j}y_s\left(k_{\eta 1}^i - k_{\eta 2}^i\right)} e^{-\mathrm{j}\left[n\sin^{-1}\left(k_{\eta 1}^i/k_0\right) - m\sin^{-1}\left(k_{\eta 2}^i/k_0\right)\right]} \mathrm{d}k_{\eta 1}^i \mathrm{d}k_{\eta 2}^i
\end{aligned} \tag{22}
$$

2.5. TE^z $\overline{\sigma_{2D}}$

As in the TM^z polarization, setting $\boldsymbol{\rho}_1 = \boldsymbol{\rho}_2 = \boldsymbol{\rho}$, substituting Eq. (12) into Eq. (22), taking the limit of Eq. (20) as $\rho \rightarrow \infty$, and subsequent simplification yields the TE^z far-zone plane-wave scattered-field spectral-density function:

$$
\begin{aligned}
S_{\mathrm{FF}}^s(\boldsymbol{\rho}, \omega) &= \frac{E_0^2 k_0}{\pi^2 \rho} \sum_{n=-\infty}^{\infty} \sum_{m=-\infty}^{\infty} R_n^{\mathrm{TE}} R_m^{\mathrm{TE}*} e^{\mathrm{j}(n-m)\phi} \\
&\quad \int_{-k_0}^{k_0} \frac{\exp\left[-\mathrm{j}(n-m)\sin^{-1}\left(k_\eta^i/k_0\right)\right]}{k_0^2 - \left(k_\eta^i\right)^2} \int_{-\infty}^{\infty} C(\eta; \ell_s) e^{\mathrm{j}k_\eta^i \eta} \mathrm{d}\eta \, \mathrm{d}k_\eta^i
\end{aligned} \tag{23}
$$

The $\overline{\sigma_{2D}}$ can be found by applying its definition provided in Eq. (14).

3. Simulation results

This section presents simulation results which serve to validate the analytical expressions derived above. Before presenting and discussing these results, a brief discussion on the simulation set-up is warranted.

3.1. Simulation set-up

The TM^z and TE^z $\overline{\sigma_{2D}}$ derived above were validated by full-wave Monte Carlo simulations. The random, correlated incident fields were generated using the phase-screen method described by Xiao and Voelz [45]. In their paper, Xiao and Voelz generate Gaussian Schell-model beams [1, 38]—a popular model for partially-coherent light. In order to compare the analytical $\overline{\sigma_{2D}}$ derived above with the well-known fully-coherent plane-wave scattering widths [6], Xiao and Voelz's phase-screen method was slightly modified to produce partially-coherent plane-wave fields which possessed Gaussian-shaped coherence functions, i.e.,

$$C(\eta;\ell_s) = e^{-\eta^2/\ell_s^2}. \tag{24}$$

Incident fields with $\ell_s = 1\lambda, 5\lambda, 10\lambda, 30\lambda$, and 50λ were generated.

Once the random plane-wave incident fields were produced, the scattering width for each incident field was computed using the MoM [4,5]. As is the common practice for two-dimensional closed structures [4, 5], systems of coupled electric and magnetic field integral equations were formulated and solved for the TM^z and TE^z polarizations, respectively. For both polarizations, pulse basis and delta testing functions were used. The basis function widths were chosen to be no greater than $\lambda/20$. Overall, 2,500 trials were used for each ℓ_s to yield the MoM $\overline{\sigma_{2D}}$. This required 12,500 MoM scattering width computations for each polarization state.

In the results presented below, the MoM $\overline{\sigma_{2D}}$ of two $a = 10\lambda$ material cylinders were computed. The first cylinder was made of aluminum, i.e., index of refraction $n = \sqrt{\varepsilon_r \mu_r} = 1.44819 - j7.5367$ at $\lambda = 632.8$ nm [46]. The second cylinder was composed of germanium, viz., $n = 4.00431$ at $\lambda = 10$ μm [46]. These materials were chosen because of their common use in constructing artificial materials.

3.2. Results

Figures 2, 3, 4, and 5 show the $\overline{\sigma_{2D}}$ results for the TM^z and TE^z polarizations for aluminum and germanium, respectively. The $\overline{\sigma_{2D}}$ results are presented on log-log plots to more clearly show the differences in the traces. For the $\overline{\sigma_{2D}}$ obtained using the analytical expressions derived in Sections 2.3 and 2.5 (dashed traces), 161 Bessel modes (i.e., sums in Eqs. (13) and (23) truncated to -80 to 80) were required for solution convergence. The bars on the MoM Monte Carlo simulation result traces denote $\pm 2\sigma_{\overline{\sigma_{2D}}}$, where $\sigma_{\overline{\sigma_{2D}}} = \sigma_{\sigma_{2D}}/\sqrt{N}$ is the standard deviation of the $\overline{\sigma_{2D}}$ calculated using $N = 2,500$ trials.

Overall, the agreement between the MoM Monte Carlo results and the theoretical $\overline{\sigma_{2D}}$ is excellent. Some interesting characteristics of the results are worth noting: First, all the aluminum traces, regardless of ℓ_s, converge to a monostatic ($\phi = 180°$) scattering width value approximately equal to πa. Note that πa is the asymptotic ($\lambda \ll a$) PEC monostatic scattering width result. For cylinders, the monostatic scattering width is a measure of the power reflected at normal incidence, i.e., the specular angle. For highly reflective and electrically large objects (such as the aluminum cylinder considered here), specular reflection does not generally depend on the coherence of the incident field.

The situation is quite different in the monostatic scattering regions of the germanium figures. Germanium, being generally translucent in the long-wave infrared, allows a significant fraction of the incident field to enter the cylinder. This interior field proceeds to reflect off and transmit
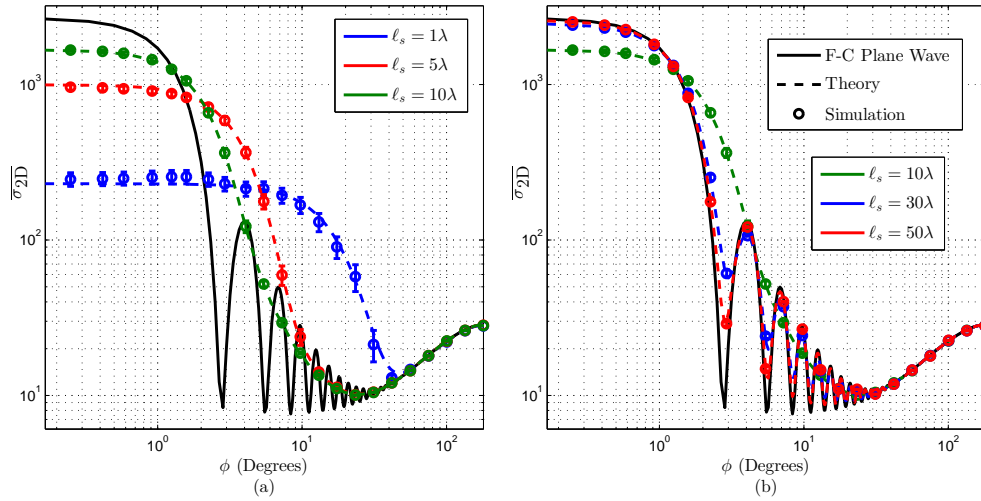
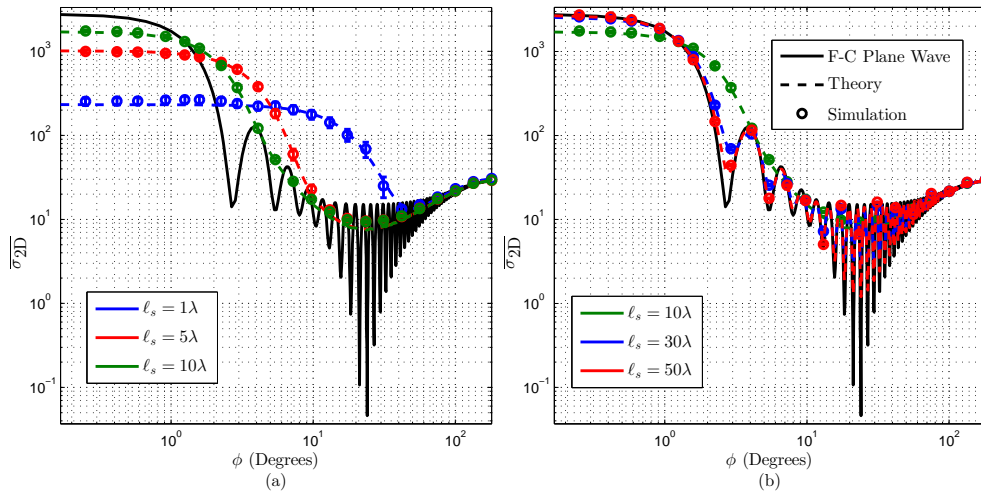Fig. 2. TM^z $\overline{\sigma_{2D}}$ results for an aluminum cylinder of radius $a = 10\lambda$. The plots compare the $\overline{\sigma_{2D}}$ obtained using the analytical expression derived in Section 2.3 (dashed traces labeled "Theory") with those obtained from the MoM Monte Carlo simulations (circles and bars labeled "Simulation"). The color of the trace denotes the value of ℓ_s. For (a), $\ell_s = 1\lambda$, 5λ, and 10λ; for (b), $\ell_s = 10\lambda$, 30λ, and 50λ. Included for reference is the scattering width for a fully-coherent plane wave (solid black trace labeled "F-C Plane Wave").

Fig. 3. TE^z $\overline{\sigma_{2D}}$ results for an aluminum cylinder of radius $a = 10\lambda$. The plots compare the $\overline{\sigma_{2D}}$ obtained using the analytical expression derived in Section 2.5 (dashed traces labeled "Theory") with those obtained from the MoM Monte Carlo simulations (circles and bars labeled "Simulation"). The color of the trace denotes the value of ℓ_s. For (a), $\ell_s = 1\lambda$, 5λ, and 10λ; for (b), $\ell_s = 10\lambda$, 30λ, and 50λ. Included for reference is the scattering width for a fully-coherent plane wave (solid black trace labeled "F-C Plane Wave").
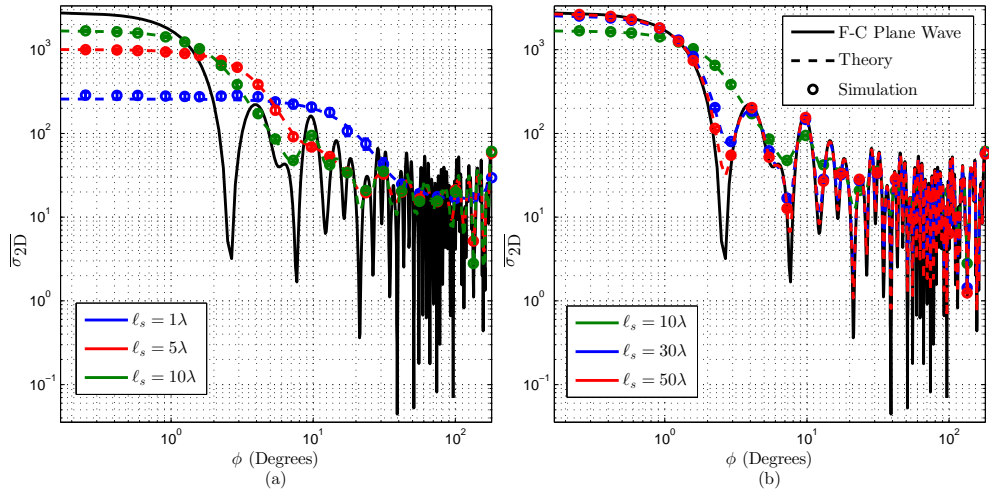
Fig. 4. TM^z $\overline{\sigma_{2D}}$ results for a germanium cylinder of radius $a = 10\lambda$. The plots compare the $\overline{\sigma_{2D}}$ obtained using the analytical expression derived in Section 2.3 (dashed traces labeled "Theory") with those obtained from the MoM Monte Carlo simulations (circles and bars labeled "Simulation"). The color of the trace denotes the value of ℓ_s. For (a), $\ell_s = 1\lambda, 5\lambda$, and 10λ; for (b), $\ell_s = 10\lambda, 30\lambda$, and 50λ. Included for reference is the scattering width for a fully-coherent plane wave (solid black trace labeled "F-C Plane Wave").
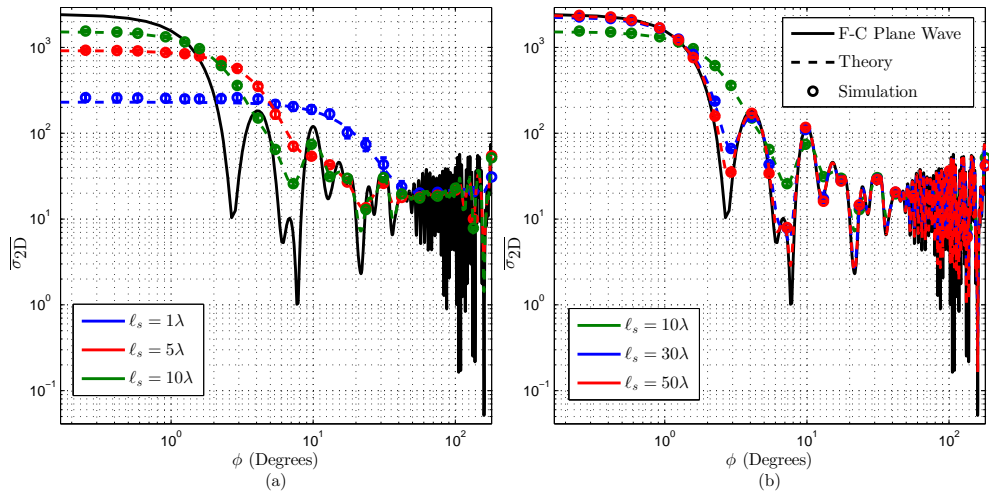

Fig. 5. TE^z $\overline{\sigma_{2D}}$ results for an germanium cylinder of radius $a = 10\lambda$. The plots compare the $\overline{\sigma_{2D}}$ obtained using the analytical expression derived in Section 2.5 (dashed traces labeled "Theory") with those obtained from the MoM Monte Carlo simulations (circles and bars labeled "Simulation"). The color of the trace denotes the value of ℓ_s. For (a), $\ell_s = 1\lambda, 5\lambda$, and 10λ; for (b), $\ell_s = 10\lambda, 30\lambda$, and 50λ. Included for reference is the scattering width for a fully-coherent plane wave (solid black trace labeled "F-C Plane Wave").
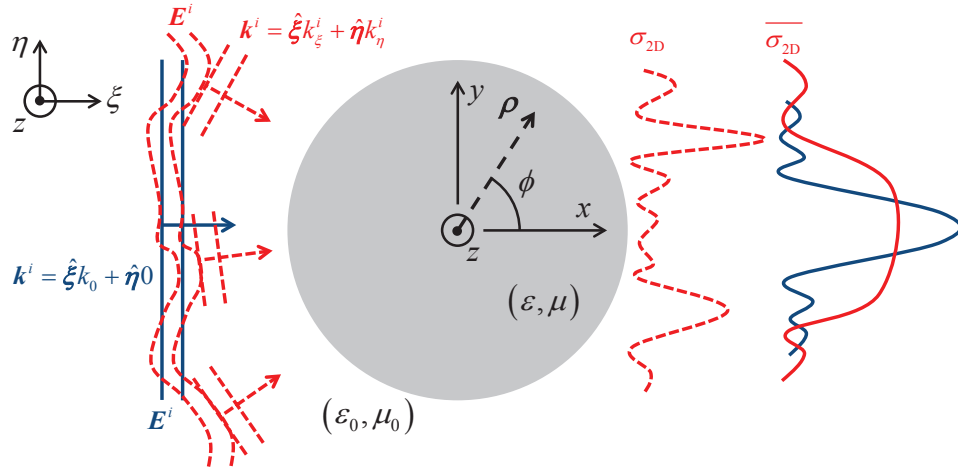
Fig. 6. Physical picture of role played by coherence in the forward scatter phenomenon. Depicted is one instance of a partially-coherent incident field (dashed red traces on left) which, when scattered from the cylinder, yields a σ_{2D} instance (dashed red trace on right). When all σ_{2D} instances are averaged, the resulting $\overline{\sigma_{2D}}$ (solid red trace) in the forward scatter direction is reduced with the forward scatter lobe subsequently broadened. To serve as a reference, the case of fully-coherent plane-wave illumination is also depicted (solid blue traces).

through the interior walls of the cylinder thereby interfering with the scattered field. This is the cause of the highly-oscillatory $\overline{\sigma_{2D}}$ results starting at about $\phi = 80°$ in Figs. 4 and 5. For the $\ell_s < 10\lambda$ traces, this region is more homogenous and is a direct consequence of the fact that incoherent fields do not interfere.

Second, as ℓ_s increases, the $\overline{\sigma_{2D}}$ converge to the classic plane-wave scattering widths. For $\ell_s < 2a$, the lobing pattern characteristic of the bistatic plane-wave scattering width is completely lost. For $\ell_s < a$, the forward scatter region is reduced in amplitude (by approximately an order of magnitude) and no longer directional. This result shows that coherence plays a significant role in the forward scatter phenomenon. Note that similar results were obtained by Fischer *et al.* [36] in their work on the scattering of partially-coherent beams from spheres. The fact that the forward scatter is reduced in magnitude and no longer directional makes the cylinder appear smaller when illuminated with partially-coherent waves. These forward scatter results make physical sense. Consider the case of a cylinder illuminated by a fully-coherent plane wave, i.e., $\boldsymbol{k}^i = \hat{\boldsymbol{\xi}} k_0 + \hat{\boldsymbol{\eta}} 0$ (solid blue traces on the left of Fig. 6). The symmetry of the cylinder combined with the coherent, uniform illumination results in constructive interference of the scattered field yielding a maximum in σ_{2D} (solid blue trace on the right of Fig. 6) in the forward scatter direction ($\phi = 0°$). Using the physical interpretation of the plane-wave spectrum representation of electromagnetic fields as a guide, partially-coherent illumination can be interpreted as the sum of infinitely-many (a continuum of) randomly-weighted plane waves incident from many angles, viz., $\boldsymbol{k}^i = \hat{\boldsymbol{\xi}} k_\xi^i + \hat{\boldsymbol{\eta}} k_\eta^i$, where $k_\xi^i > 0$ and, in general, $k_\eta^i \neq 0$ (dashed red traces on the left of Fig. 6). When scattered from the cylinder, the sum, or integral of the plane-wave components of the partially-coherent incident field produces a σ_{2D} instance (dashed red trace on the right of Fig. 6). The maxima of this σ_{2D} instance are, in general, located at angles other than $\phi = 0°$. When all instances of σ_{2D} are averaged, the resulting $\overline{\sigma_{2D}}$ in the forward scatter direction is reduced with the forward scatter lobe subsequently broadened (solid red trace in Fig. 6).

Last, for all but the least coherent ℓ_s cases, the bar widths on the simulation traces are negligible implying statistical convergence of $\overline{\sigma_{2D}}$. The others, namely, $\ell_s = 1\lambda$ and 5λ, would require many more trials to reach the confidence levels of the other ℓ_s simulations. This is physically expected since generating nearly incoherent incident fields necessitates using very strong phase screens [45]. This requires many trials, in this case many more than 2,500, to achieve statistical convergence. Although the $\ell_s = 1\lambda$ and 5λ $\overline{\sigma_{2D}}$ do not achieve the confidence levels of the other ℓ_s cases, the corresponding analytical traces lie within the bars giving credence to the validity of the theoretical $\overline{\sigma_{2D}}$ expressions for these tough cases.

4. Conclusions

The scattering of a partially-coherent wave from a material cylinder was investigated. Expressions for the TM^z and TE^z scattered-field CSD functions were derived. This was accomplished by first writing the partially-coherent incident fields in terms of their plane-wave spectrums. The resulting incident-field expressions were then expanded in terms of cylindrical wave functions. Transverse field boundary conditions were then enforced at the surface of the cylinder to yield relations for the unknown cylindrical wave function coefficients. From these, moments of the scattered fields were derived including the desired CSD functions, the spectral densities, and the mean scattering widths. These relations were also physically interpreted.

To validate the TM^z and TE^z analytical solutions, MoM Monte Carlo simulations were performed to compute $\overline{\sigma_{2D}}$ of $a = 10\lambda$ aluminum and germanium cylinders. The simulations tested the analytical relations over a wide range of incident-field spatial-coherence radii ℓ_s, spanning from nearly fully-coherent ($\ell_s \gg a$) to incoherent ($\ell_s \ll a$) cases. Overall, the agreement between the theoretical and simulation results was excellent. For the highly reflective and electrically large aluminum cylinder, the results showed that the monostatic scattering width was independent of the coherence of the incident field. On the other hand, the monostatic scattering width demonstrated a rather strong dependence on the coherence of the incident field in the case of the translucent germanium cylinder. Last, the forward scatter regions of both the aluminum and germanium cylinders were significantly reduced in magnitude and directionality as $\ell_s \to 0$. This result shows that coherence plays a significant role in the forward scatter phenomenon.